

The effect of Galactic foreground subtraction on redshifted 21-cm observations of quasar HII regions

Paul. M. Geil^{1*}, J. Stuart B. Wyithe¹, Nada Petrovic², S. Peng Oh²

¹*School of Physics, University of Melbourne, Parkville, Victoria, Australia*

²*Department of Physics, University of California, Santa Barbara, CA 93106, USA.*

24 March 2021

ABSTRACT

We assess the impact of Galactic synchrotron foreground removal on the observation of high-redshift quasar HII regions in redshifted 21-cm emission. We consider the case where a quasar is observed in an intergalactic medium (IGM) whose ionisation structure evolves slowly relative to the light crossing time of the HII region, as well as the case where the evolution is rapid. The latter case is expected towards the end of the reionisation era where the highest redshift luminous quasars will be observed. In the absence of foregrounds the fraction of neutral hydrogen in the IGM could be measured directly from the contrast between the HII region and surrounding IGM. However, we find that foreground removal lowers the observed contrast between the HII region and the IGM. This indicates that measurement of the neutral fraction would require modelling to correct for this systematic effect. On the other hand, foreground removal does not modify the most prominent features of the 21-cm maps. Using a simple algorithm we demonstrate that measurements of the size and shape of observed HII regions will not be affected by continuum foreground removal. Moreover, measurements of these quantities will not be adversely affected by the presence of a rapidly evolving IGM.

Key words: cosmology: diffuse radiation, large-scale structure, theory – galaxies: high redshift, intergalactic medium

1 INTRODUCTION

The reionisation of cosmic hydrogen by the first stars and galaxies was an important milestone in the history of the Universe (e.g. Barkana & Loeb 2001). A powerful tool for study of the reionisation history will be provided by the redshifted 21-cm emission from neutral hydrogen in the intergalactic medium (IGM), and several probes of the reionisation era in redshifted 21-cm emission have been suggested. These include observation of the emission as a function of redshift averaged over a large area of sky. This observation would provide a direct probe of the evolution in the neutral fraction of the IGM, and is referred to as the global step (Shaver et al. 1999; Gnedin & Shaver 2004; Furlanetto 2006). Unless reionisation is uniform throughout the whole IGM however, the global step will be very difficult to detect beneath the bright foreground. A more powerful probe will be provided by observation of the 21-cm power spectrum of fluctuations together with its evolution with redshift. This observation would trace the evolution of neutral gas with redshift as well as the topology of the reionisation process

(e.g. Tozzi et al. 2000; Furlanetto et al. 2004; Loeb & Zaldarriaga 2004; Wyithe & Morales 2007; Iliev et al. 2006). Finally, observation of individual HII regions will probe quasar physics as well as the evolution of the neutral gas (Wyithe & Loeb 2004; Kohler et al. 2005; Valdés et al. 2006). Kohler et al. (2005) have generated synthetic spectra using cosmological simulations and conclude that quasar HII regions will provide the most prominent individual cosmological signals. Work by Datta et al. (2007) has focused on the detection of ionised bubbles in redshifted 21-cm maps. Their results suggest it may be possible to blindly detect spherical HII regions of radius $\gtrsim 22$ comoving Mpc during the epoch of reionisation. More recently, Geil & Wyithe (2007) (hereafter GW07) have studied the impact of a percolating IGM on the detection of HII regions, and shown that quasars will leave a detectable imprint until very late in the reionisation era.

Various experiments are planned to measure 21-cm emission from the pre-reionisation IGM, including the Low Frequency Array¹ (LOFAR) and the Murchison Widefield Array² (MWA). In addition to their physical configuration,

* Email: pgeil@physics.unimelb.edu.au

¹ <http://www.lofar.org/>

² <http://www.haystack.mit.edu/ast/arrays/mwa/>

the sensitivity of these telescopes to the epoch of reionisation will be limited by the difficulty of achieving a perfect calibration and by problems associated with foregrounds and the ionosphere. There has been significant discussion in the literature regarding low-frequency foregrounds. While fluctuations due to foregrounds are expected to be orders of magnitude larger than the reionisation signal (e.g. Di Matteo et al. 2002; Oh & Mack 2003), foreground spectra are anticipated to be smooth. Since the reionisation signature includes fluctuations in frequency as well as angle, it has therefore been proposed that they be removed through continuum subtraction (e.g. Gnedin & Shaver 2004; Wang et al. 2006), or using the differences in symmetry from power spectra analysis (Morales & Hewitt 2004; Zaldarriaga et al. 2004).

In this paper we focus on the observation of individual HII regions around known quasars, with emphasis on the capabilities of the MWA. In particular we address the removal of a bright Galactic foreground from the redshifted 21-cm signal. Our analysis extends the model and ideas presented in GW07 by including evolution of the percolating IGM. We begin by summarising our semi-numerical model for the ionisation structure of the IGM (§2). We show examples of model HII regions in §3 (both with and without evolution of the IGM). We then discuss the influence of foregrounds in §4 and describe the observation of the HII region with a low-frequency array in §5, including discussion of foreground removal and reconstruction of the HII region shape. The effects of different foreground removal models on HII region observables are investigated in §6. We present our conclusions in §7. Throughout we adopt the set of cosmological parameters determined by WMAP (Spergel et al. 2007) for a flat Λ CDM universe.

2 SEMI-NUMERICAL MODEL FOR THE GROWTH OF QUASAR HII REGIONS IN A PERCOLATING IGM

In this section we describe our model for the reionisation of a three-dimensional volume of the IGM using a semi-numerical scheme (Geil & Wyithe 2007; Zahn et al. 2007; Mesinger & Furlanetto 2007). We follow the implementation described in GW07, and refer the reader to that paper for details of the model. The model employs a semi-analytic prescription for the reionisation process, which is combined with a realisation of the density field. Each of these aspects is summarised briefly below.

2.1 Density-dependent model of global reionisation

The semi-analytic component of our model computes the relation between the local dark matter overdensity and the reionisation of the IGM, and is based on the model described by Wyithe & Loeb (2007) and Wyithe & Morales (2007). The model includes the overabundance of galaxies in overdense regions that results from galaxy bias (Mo & White 1996), as well as the increase in the recombination rate in overdense regions, and ionisation feedback which suppresses low-mass galaxy formation in ionised regions. This model predicts the sum of astrophysical effects to be dominated by galaxy bias, and that as a result, overdense regions are

reionised first. This leads to the growth of HII regions via a phase of percolation during which individual HII regions overlap around clustered sources in overdense regions of the universe. The output of the semi-analytic model is evolution of the ionisation fraction by mass $Q_{\delta,R}$ of a particular region of scale R with overdensity δ .

Throughout this paper we consider a model in which the mean IGM is reionised at $z = 6$ (Fan et al. 2006; Gnedin & Fan 2006; White et al. 2003). We assume that star formation proceeds in halos above the hydrogen cooling threshold in neutral regions of IGM. In ionised regions of the IGM star formation is assumed to be suppressed by radiative feedback.

2.2 The ionisation field

We construct an ionisation field based on a Gaussian random field for the matter overdensity, combined with the value of the ionised fraction $Q_{\delta,R}$ as a function of overdensity and smoothing scale. We repeatedly filter the linear density field at logarithmic intervals on scales comparable to the box size down to the grid scale size. For all filter scales, the ionisation state of each grid position is determined using $Q_{\delta,R}$ and deemed to be fully ionised if $Q_{\delta,R} \geq 1$. All voxels within a sphere of radius R centered on these positions are flagged and assigned $Q_{\delta,R} = 1$, while the remaining non-ionised voxels are assigned an ionised fraction of $Q_{\delta,R_{f,\min}}$, where $R_{f,\min}$ corresponds to the smallest smoothing scale. A voxel forms part of an HII region if $Q_{\delta,R} > 1$ on any scale R . In this paper we present simulations corresponding to a linear density field of resolution 256^3 , with a comoving side length of 512 Mpc. We label positions within the simulation with the vector $\mathbf{x} = (x_1, x_2, x_3)$, and define the center of the box as the origin. We take the x_3 -axis to be parallel to the line of sight, and show results using dimensions of proper distance. The line-of-sight coordinate (x_3) can be equivalently described using redshift or frequency. We have chosen the side length of 512 comoving Mpc to match the 32 MHz bandpass of the MWA, centered on a quasar at $z = 6.65$.

2.3 The evolution of quasar HII regions in a percolating IGM

A semi-numerical simulation generates a realisation of the three-dimensional ionisation field at a particular value of proper time (GW07). However, late in the reionisation era, where we expect to observe the high-redshift quasars, the light travel time across a quasar HII region may be comparable to the timescale over which the IGM evolves significantly. This evolution may have a negative impact on the observability of quasar HII regions. In this paper we therefore describe semi-numerical calculations of an ionisation field for two different cases of IGM evolution. In the first we assume a non-evolving IGM with a slowly evolving quasar. In the second we consider a model where the line-of-sight axis includes the finite light travel time, and evolution of the IGM ionisation and quasar luminosity. The first case corresponds to the model in GW07. The additions to this model that are required for the second case (with an evolving IGM) are as follows.

Unlike an N -body simulation which evolves an ionisation field in time, a semi-numerical calculation computes the

ionisation field at a single instant in time. To include the finite speed of light we must therefore compute many simulations at closely separated redshifts and stack slices with line-of-sight distances such that the photons from all slices reach the observer at the same time. The redshift of a slice is

$$z \approx z_0 + \left(\frac{cdt}{dz} \right)^{-1} (x_3 - x_3^0), \quad (1)$$

where x_3 is the proper distance coordinate along the line of sight, and x_3^0 is proper the distance to redshift z_0 .

2.4 Inclusion of quasars in the semi-numerical scheme

In this section we describe the effect of the quasar on the evolving ionisation structure of the IGM. The quasar has an influence which evolves with time. We assume the quasar turns on(off) at a redshift $z_{\text{on(off)}}$ (corresponding to a proper time $t_{\text{on(off)}}$), and has a lifetime $t_{\text{lt}} = t_{\text{off}} - t_{\text{on}}$. Following the calculation in GW07 we parameterise the influence of the quasar using the distance R_{q} , which is the radius of the region that would have been ionised by the quasar alone in a fully neutral IGM

$$R_{\text{q}} = \begin{cases} 0 & z > z_{\text{on}} \\ R_{\text{q,tot}} (t/t_{\text{on}})^{1/3} & z_{\text{off}} < z < z_{\text{on}} \\ R_{\text{q,tot}} & z < z_{\text{off}}, \end{cases} \quad (2)$$

where $R_{\text{q,tot}}$ is the maximum radius of the HII region that would have been generated by the quasar in a fully neutral IGM.

To include the influence of a quasar in an evolving IGM we generate an ionisation cube for the IGM as a function of look-back time using the procedure described above. However in doing so we use equation (2) to include the time-dependent quasar contribution to the ionising photon budget. In a region of radius R containing a quasar, the cumulative number of ionisations per baryon will be larger than predicted by the semi-analytic model. We include quasars in our scheme by first computing the fraction of the IGM within a region of radius R centered on the position \mathbf{x} that has already been ionised by stars. We then add an additional ionisation fraction equal to the quasar's contribution

$$Q_{\text{q}}(\mathbf{x}) = \left(\frac{|\mathbf{x} - \mathbf{x}_{\text{q}}|}{R_{\text{q}}} \right)^{-3}, \quad (3)$$

where \mathbf{x}_{q} is the position of the quasar, and R_{q} is computed via equation (2). In contrast to stellar ionisation the quasar contribution comes from a point source, and so the contribution to Q originates from a single voxel only (rather than all voxels within $|\mathbf{x} - \mathbf{x}_{\text{q}}|$). Following this addition we filter the ionisation field as described in §2.2.

The value of $R_{\text{q,tot}}$ is subject to large uncertainties, including the quasar duty cycle, lifetime and luminosity. Assuming a line-of-sight ionising photon emission rate of $\dot{N}_{\gamma}/4\pi$ photons per second per steradian, a uniform IGM and neglecting recombinations, the comoving line-of-sight extent of a quasar's HII region (from the quasar to the *front* of the region) observed at time t is (White et al. 2003)

$$R_{\text{q,tot}} \approx 30 \text{ Mpc } x_{\text{HI}}^{-1/3} \left(\frac{\dot{N}_{\gamma}}{10^{57}} \frac{t_{\text{lt}}}{10^7 \text{ yr}} \right)^{1/3} \left(\frac{1+z}{7.5} \right)^{-1}, \quad (4)$$

where x_{HI} is the neutral fraction. In this paper we show examples of $R_{\text{q,tot}} \approx 34$ comoving Mpc, consistent with the lower limit around the luminous SDSS quasars at $z > 6$ (Fan et al. 2006).

3 EXAMPLES OF QUASAR HII REGIONS

We compute the three-dimensional ionisation structure for our reionisation model using the prescription outlined in §2. The contrast in 21-cm brightness temperature corresponding to a region in the simulation with ionisation fraction Q and overdensity δ is

$$T(\delta, R) = 22 \text{ mK } (1 - Q_{\delta, R}) \left(\frac{1+z}{7.5} \right)^{1/2} (1 + \delta). \quad (5)$$

Here we have assumed that the spin-temperature of neutral hydrogen in the IGM is much larger than the cosmic microwave background (CMB) temperature (Ciardi & Madau 2003), and ignored the enhancement of the brightness temperature fluctuations due to peculiar velocities in overdense regions (Bharadwaj & Ali 2005; Barkana & Loeb 2005). Because the ionisation state of the IGM around the highest redshift quasars is not known, we consider the two cases described in §2.3 which bracket the ionisation conditions surrounding a quasar prior to the completion of reionisation.

Resulting 21-cm brightness temperature maps are presented in Figures 1–3. In the upper row of Figure 1 we show snapshots of the model brightness temperature T_{model} for slices through a realisation at a time when the mean neutral fraction of the IGM is $\approx 15\%$, corresponding to redshift $z = 6.65$ (assuming $R_{\text{q}} = R_{\text{q,tot}}$). This simulation was computed at fixed proper time, and so represents the model with slow evolution in the reionisation process. Each slice is 3 comoving Mpc deep. We show three aspects of the HII region, with slices viewed from the front, side and top. These slices are similar because the simulation is statistically isotropic. The position of the quasar within the simulation cube is plotted as a square point.

In Figures 2 and 3 we show results for the model in which finite light-travel time is included, showing the effect of rapid evolution in the ionisation state of the IGM towards the end of the reionisation era. In this simulation the center of the box is at $z = 6.65$, at which time the IGM has a neutral fraction of $\approx 15\%$. The quasar is assumed to have $R_{\text{q,tot}} = 34$ comoving Mpc, a lifetime of 2×10^7 yr and be centered on $z = 6.65$. The position of the quasar within the simulation cube is plotted as a square point. The upper row of Figure 2 shows three aspects of the HII region in this model, with slices viewed from the front, side and top. The evolution of the IGM is clearly seen in this figure, with the percolation process completing between the “back” of the box ($x_3 > 0$) and the “front” of the box ($x_3 < 0$). In Figure 3 we show a sequence of slices between $z = 6.74$ and 6.56. These slices show the thinning of neutral gas towards lower redshifts. The presence of an HII region around the quasar can be seen towards the middle of the redshift range.

4 THE CONTINUUM FOREGROUND

Foreground contamination and its removal could have significant consequences for the detectability of the weak, red-

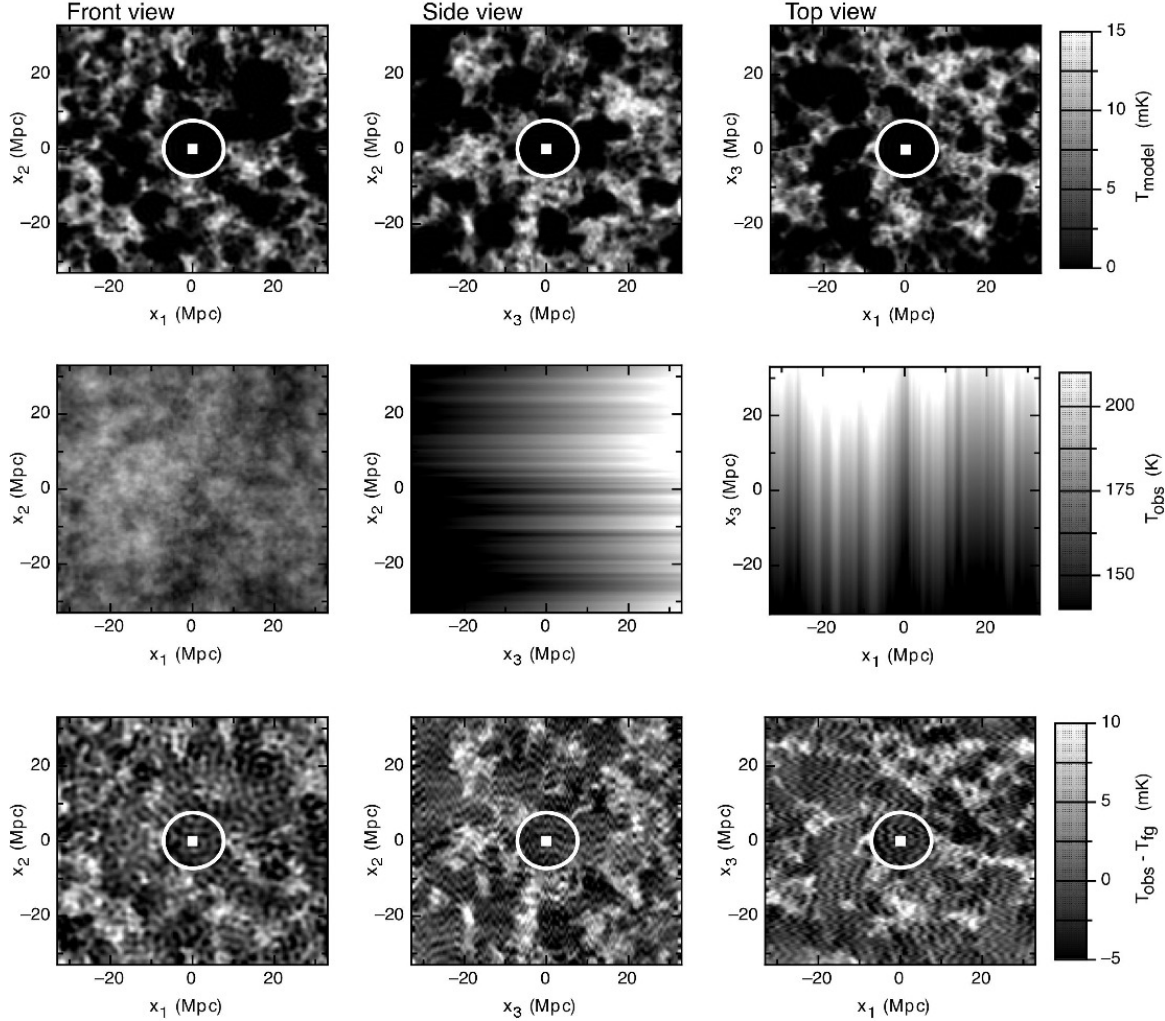


Figure 1. A quasar HII region in a non-evolving IGM. Three aspects of the HII region are shown, with slices through the center of the box when viewed from the front, top and side. Each slice is 6 Mpc thick, which corresponds to ~ 3 MHz along the x_3 -axis. In observed units, the cube is ~ 3.3 degrees on a side and 33 MHz deep. The model, foreground plus model, and observed maps following foreground removal are shown in the upper, central and lower panels respectively. The shape of the HII region extracted from the foreground removed cubes using the method described in the text are also plotted. The quasar was assumed to have $R_{q,tot} = 34$ comoving Mpc, and its position is plotted as the square point. The mass-averaged IGM neutral fraction is assumed to be 15%. For the purposes of display we have used the central redshift of the box to convert between proper and comoving distances throughout this paper.

shifted 21-cm signal. Indeed foreground contamination will be brighter than the cosmological 21-cm signal by 4–5 orders of magnitude. The three main sources of foreground contamination of the 21-cm signal are Galactic synchrotron (which comprises $\sim 70\%$), extragalactic point sources (27%) and Galactic bremsstrahlung (1%) (Shaver et al. 1999). The frequency dependence of these foregrounds can be approximated by power laws with a running spectral index (Shaver et al. 1999; Tegmark et al. 2000). While the sum of power laws is not in general a power law, over a relatively narrow frequency range (such as that considered in this paper where $\Delta\nu/\nu \ll 1$), a Taylor expansion around a power law can be used to describe the spectral shape. We therefore also approximate the sum of foregrounds as a power law with a running spectral index, and specialise to the case of Galac-

tic synchrotron emission, which dominates the foregrounds³. For more detailed foreground models, including synchrotron emission from discrete sources such as supernova remnants, and free-free emission from diffuse ionised gas, see Jelic et al. (2008). We assume that the brightest point sources have been removed and only consider unpolarised foregrounds.

³ The primary effect of other foregrounds will be to slightly alter the spectral index and the frequency dependence of the spectral index, and also (in the case of unresolved radio point sources) the angular structure of the foreground at small scales. Neither of these effects is important as our foreground removal technique is not sensitive to the specific value of the spectral index we adopt. As for angular fluctuations, these correspond to zero-point fluctuations along different lines of sight, which are immediately removed by foreground cleaning. We have experimented with increasing angular fluctuations by a factor of 10, and found little difference.

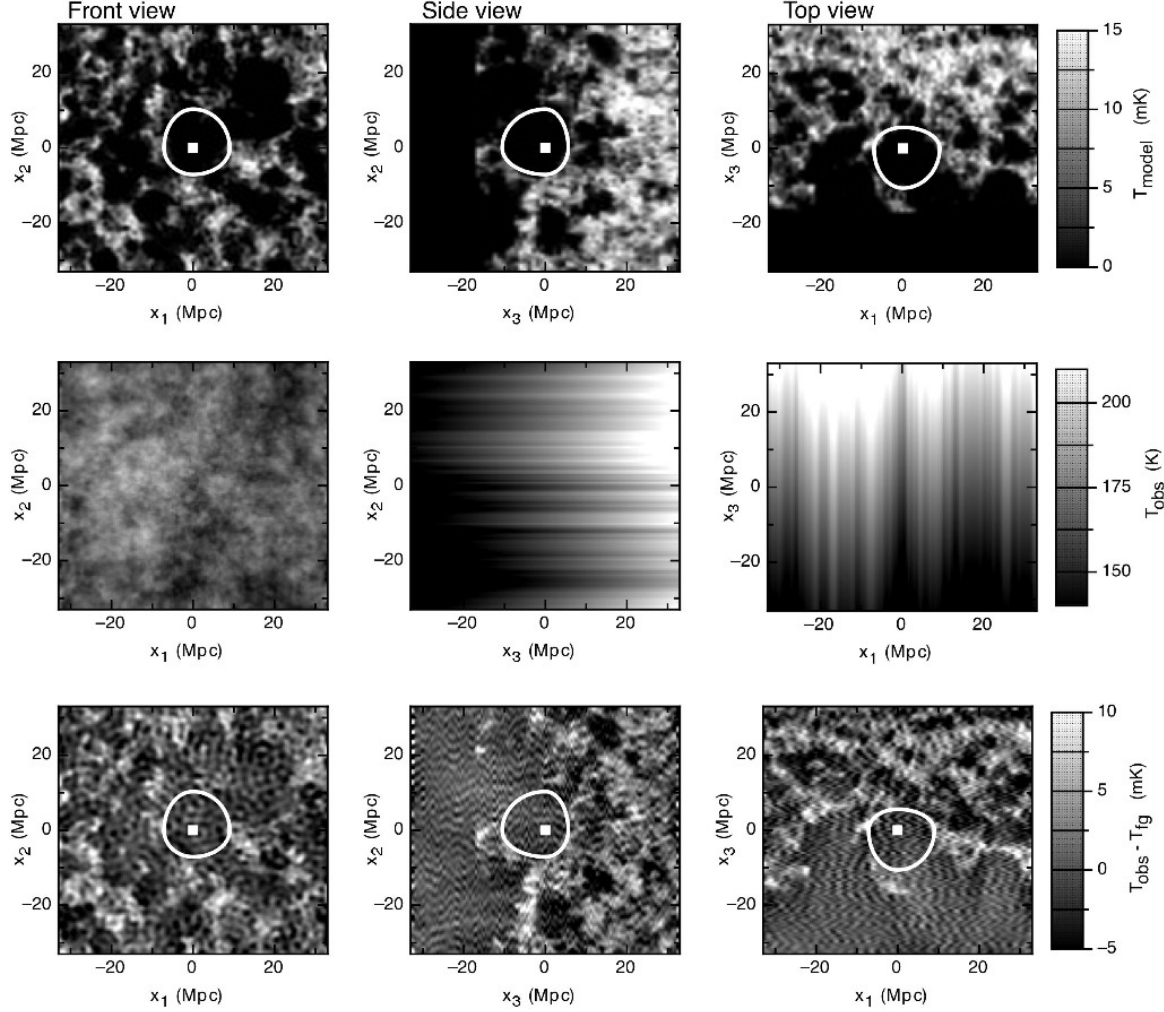


Figure 2. As per Figure 1, this time for a quasar in an evolving IGM. The quasar was assumed to have $R_{q,tot} = 34$ comoving Mpc and a lifetime of 4×10^7 yr centered on $z = 6.65$, which is also the redshift at the center of the simulation box. The mass-averaged IGM neutral fraction at the redshift of the quasar is $\approx 15\%$.

The intensity of Galactic synchrotron emission varies as a function of both sky position and frequency. We model the frequency and angular dependence of Galactic synchrotron foreground emission as follows. We first construct a realisation of the angular fluctuations in the foreground (around the mean brightness temperature) at a particular frequency ν_0 using the relation

$$\frac{l^2 C_l(\nu_0)}{2\pi} = \left(\frac{l}{l_0}\right)^{2-\beta} T_{l_0}^{\text{syn}}(\nu_0)^2, \quad (6)$$

where the frequency dependence of the fluctuation amplitude is given by

$$T_{l_0}^{\text{syn}}(\nu_0) = A_{l_0}^{\text{syn}} \left(\frac{\nu_0}{150 \text{ MHz}}\right)^{-\alpha_{\text{syn}} - \Delta\alpha_{\text{syn}} \log_{10}[\nu_0/(150 \text{ MHz})]}, \quad (7)$$

and the constants have values $\alpha_{\text{syn}} = 2.55$, $\Delta\alpha_{\text{syn}} = 0.1$ and $A_{l_0}^{\text{syn}} = 25$ K (Shaver et al. 1999; Tegmark et al. 2000; Wang et al. 2006). The latter two values are extrapolated from 30 GHz CMB observations (McQuinn et al. 2006) since at present there are no data at lower frequencies with arc

minute resolution⁴. We then add a mean sky brightness $\bar{T}^{\text{syn}} = 165 (\nu_0/185 \text{ MHz})^{-2.6}$ K to our two-dimensional realisation of brightness temperature fluctuations $\Delta T^{\text{syn}}(\theta)$ (although interferometers will generally not be sensitive to the temperature zero-point). This foreground plane is then extended into three dimensions by extrapolation, using the running power law form along each line of sight

$$T^{\text{syn}}(\theta, \nu) = [\bar{T}^{\text{syn}} + \Delta T^{\text{syn}}(\theta)] \left(\frac{\nu}{\nu_0}\right)^{-\alpha_{\text{syn}} - \Delta\alpha_{\text{syn}} \log_{10}[\nu/\nu_0]}. \quad (8)$$

⁴ Although the high frequencies of CMB experiments make them less than ideal for understanding diffuse Galactic emission at frequencies relevant to high-redshift 21-cm tomography, several publicly available unpolarised, large area radio surveys have been compiled to form a Global Sky Model (see e.g. <http://space.mit.edu/~angelica/gsm/index.html>). This, together with the 843 MHz sub-degree resolution and ~ 1 Jy beam⁻¹ rms sensitivity SUMMS survey (Bock et al. 1999) for $\delta < -30^\circ$, will provide a better practical continuum foreground model for the MWA target fields (Randall Wayth, private communication).

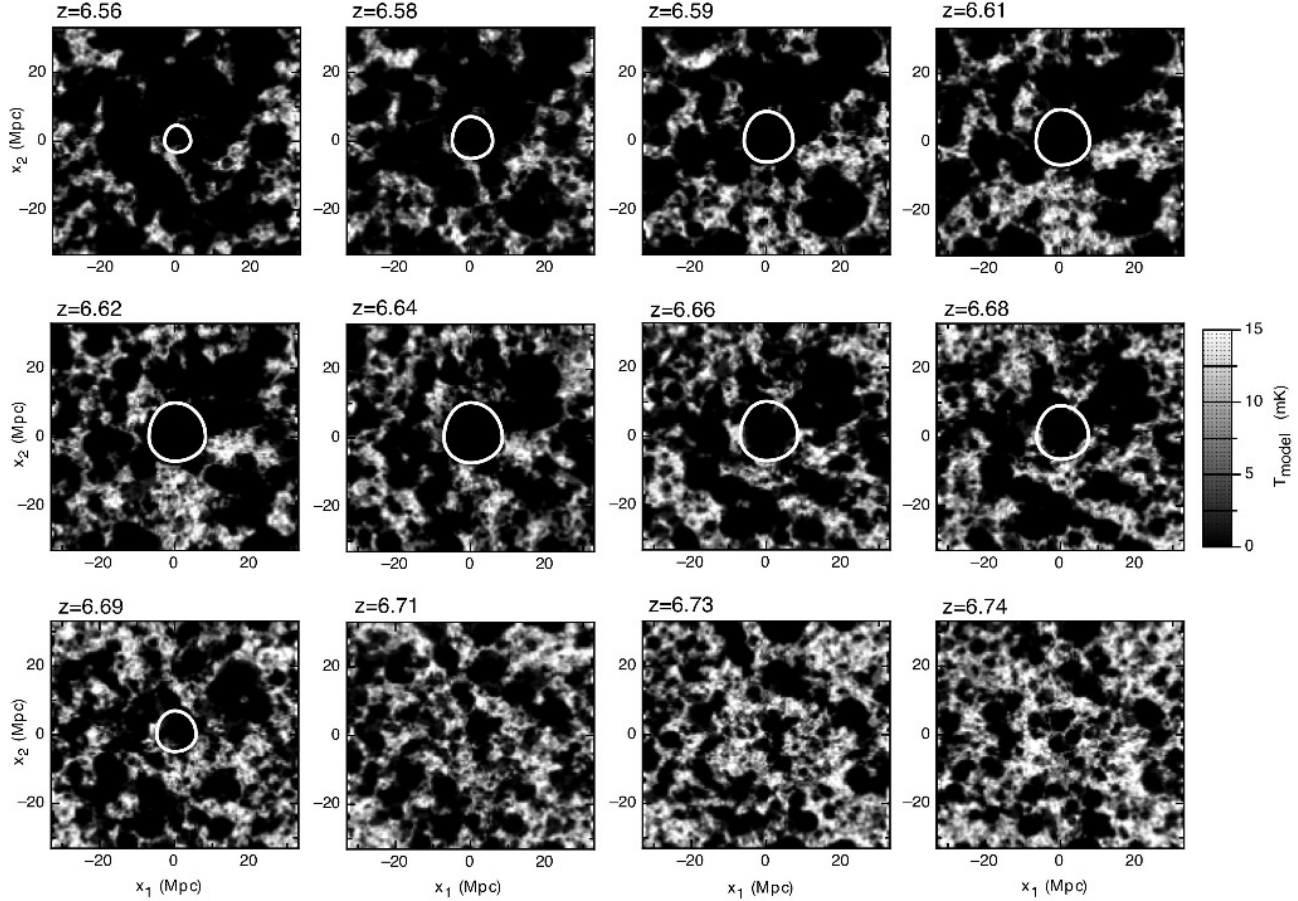


Figure 3. Slices through the simulation of a quasar in an evolving IGM for $6.56 \leq z \leq 6.74$, viewed from the front. The shapes of the HII regions extracted from foreground removed cubes using the method described in the text are also plotted.

In this paper we have not modeled the spatial variation of α and $\Delta\alpha_{\text{syn}}$, although the effect of this is negligible, as we have verified in other work (Petrovic & Oh, 2008, in preparation). Most of the error in foreground fitting comes from “noise” due to the instrument and the cosmological 21-cm signal.

The total observed brightness temperature becomes $T_{\text{obs}} = T^{\text{syn}} + T_{\text{model}}$. Maps of the continuum foreground model plus 21-cm signal are shown in the second row of panels in Figures 1 and 2. The foreground completely swamps the HII region signal, which is not visible in the combined maps. The mean and variance of the foreground brightness (at the central frequency of these cubes) are 1.7×10^5 mK and 8.7×10^3 mK respectively, which should be compared to the ~ 10 mK 21-cm fluctuations. The front, side and top views are shown as before. The front view shows the angular structure of the foreground, while the side and top views show the coherent structure along the line of sight, owing to the smooth frequency dependence of the assumed foreground emission.

5 SYNTHETIC OBSERVATIONS OF MODEL HII REGIONS

In this section we discuss the response of a low-frequency array to the model HII regions described in §3, including

foreground subtraction. We then estimate the potential for measurement of HII region properties, including the HII region shape and the global neutral fraction.

5.1 Fundamental sensitivity limit to the 21-cm signal

To compute the response of a low-frequency array to the model HII region we follow the prescription given in GW07. Radio interferometers measure a frequency-dependent, complex visibility $V(\mathbf{U}, \nu)$ (Jy) for each frequency channel and baseline \mathbf{U} in their configuration. The measured visibility is, in general, a linear combination of signal, foreground and system noise,

$$V(\mathbf{U}, \nu) = V_{\text{S}}(\mathbf{U}, \nu) + V_{\text{F}}(\mathbf{U}, \nu) + V_{\text{N}}(\mathbf{U}, \nu), \quad (9)$$

where V_{S} is the signal, V_{F} the contribution due to foreground sources and V_{N} the system noise. The root mean square of noise fluctuation per visibility per frequency channel is given by

$$\Delta V_{\text{N}} = \frac{2k_{\text{B}}T_{\text{sys}}}{A_{\text{eff}}\sqrt{t_{\text{U}}\Delta\nu}}, \quad (10)$$

where T_{sys} is the system temperature (K), A_{eff} the effective area of one antenna (m^2), t_{U} is the integration time for that visibility (s), $\Delta\nu$ is the frequency bin width (Hz) and k_{B} is

the Boltzmann constant. Instrumental noise is uncorrelated in the frequency domain and is assumed to be Gaussian. As shown by McQuinn et al. (2006), the average integration time $t_{\mathbf{U}}$ that an array observes the visibility \mathbf{U} is

$$t_{\mathbf{U}} \approx \frac{A_{\text{eff}} t_{\text{int}}}{\lambda^2} n(\mathbf{U}), \quad (11)$$

where t_{int} is the total integration time and $n(\mathbf{U})$ is the number density of baselines that can observe the visibility \mathbf{U} . The transverse wavenumber k_{\perp} is given by $k_{\perp} = 2\pi|\mathbf{U}|/r_{\text{em}}(z)$, where $r_{\text{em}}(z)$ is the proper distance to the point of emission.

We present simulated results for the MWA, which will consist of 512 tiles, each with 16 cross-dipoles with 1.07 m spacing and an effective area $A_{\text{eff}} \approx 16(\lambda^2/4)$ for $\lambda \lesssim 2.1$ m. The system temperature at $\nu < 200$ MHz is sky dominated and has a value $T_{\text{sys}} \sim 250[(1+z)/7]^{2.6}$ K. This value is an estimate of the average sky brightness due to Galactic synchrotron emission over the primary beam. Following Bowman et al. (2006), we assume a smooth antenna density profile $\rho_{\text{ant}} \propto r^{-2}$ within a 750 m radius. For the MWA, the aperture is filled within a radius of 18 m. In order to maintain high sensitivity we truncate the naturally weighted visibility data using a filled circular aperture of radius a with a corresponding beamwidth (full width at half maximum) $\theta_{\text{b}} = 0.705U_{\text{max}}^{-1}$, where $U_{\text{max}} = a/\lambda$. In this paper we show results computed for $\theta_{\text{b}} = 3.2'$, and assume an integration time of $t_{\text{int}} = 100$ hours.

We simulate the thermal noise in a three-dimensional visibility-frequency cube using equations (10) and (11), allowing us to account for a particular array configuration and observation strategy. We then perform a two-dimensional inverse Fourier transform in the uv -plane for each frequency channel in the bandwidth, which gives a realisation of the system noise in the image cube (i.e. sky coordinates). Using the linearity of both the Fourier transform and equation (9), the observed specific intensity can then be found either by first adding visibility terms and then transforming to image space, or by adding the realisation of each visibility component in image space. Finally, we apply the Rayleigh-Jeans approximation to express the observed flux in terms of brightness temperature T using $\partial B_{\nu}/\partial T = 2k_{\text{B}}/\lambda^2$, where B_{ν} is the specific intensity.

5.2 Continuum foreground subtraction

It has been suggested that spectrally smooth foregrounds could be removed through continuum subtraction (Gnedin & Shaver 2004; Wang et al. 2006; Jelic et al. 2008). We model the continuum using a polynomial of the form

$$\log_{10}(T_{\text{fg}}) = \sum_{i=0}^{n_{\text{log}}} C_i [\log_{10}(\nu)]^i, \quad (12)$$

where ν is the observed frequency⁵. We begin with results for $n_{\text{log}} = 3$ (which we label model II), but return to discuss different foreground removal models in § 6.

We perform a fit of this functional form along the

⁵ Note that when compared with the frequency evolution assumed for our synchrotron model, the coefficients C_1 and C_2 correspond to α_{syn} and $\Delta\alpha_{\text{syn}}$ respectively.

Table 1. Parameters describing the HII region shape in models of non-evolving and evolving IGM, corresponding to Figures 1 and 2 respectively. The values in parentheses are the offset relative to the volume-averaged radius $\langle R^3 \rangle^{1/3}$.

	evolving IGM		non-evolving IGM	
	FGR map	model	FGR map	model
A_1	7.1 (-1.7)	7.0 (-1.6)	7.1 (-0.2)	6.8 (-0.6)
A_2	9.0 (+0.2)	8.4 (-0.2)	7.6 (+0.1)	7.6 (+0.2)
B_1	7.1 (-1.7)	7.4 (-1.2)	7.3 (-0.1)	7.3 (-0.1)
B_2	10.3 (+1.5)	10.4 (+1.8)	7.6 (+0.2)	7.5 (+0.1)
C_1	11.0 (+2.2)	10.5 (+1.9)	7.1 (-0.3)	7.4 (0.0)
C_2	5.6 (-3.2)	5.6 (-3.0)	7.6 (+0.5)	7.6 (+0.2)
$\langle R^3 \rangle^{1/3}$	8.8	8.6	7.4	7.4

line of sight to each spatial pixel in the simulation cube. We then subtract the best-fit, leaving residual fluctuations around the foreground emission. The resulting foreground subtracted maps are plotted in the lower rows of Figures 1 and 2. Inspection of these maps indicates that the main features of the HII regions are still present. However, foreground removal has significantly lowered the contrast of the maps relative to the input model. This is because foreground removal erases modes in the signal with wavelengths comparable to the bandpass, leaving a foreground-cleaned data cube composed of residuals, with a near zero-mean brightness temperature.

5.3 The shape of HII regions

In our model we have assumed isotropic quasar emission, which is probably not correct. However even in this case the resulting HII region may not be spherical owing to the inhomogeneous nature of the stellar reionisation around the quasar HII region, as well as the effects of evolution which could serve to elongate the HII region along the line of sight (Wyithe et al. 2005; Yu 2005).

In an inhomogeneously ionised IGM the meaning of “shape” is not clear. For the purpose of illustration, we define the shape of the HII region to be the shape of a spheroid that maximises the contrast in 21-cm emission,

$$T_{\text{contrast}} = \langle T_{\text{out}} \rangle - \langle T_{\text{in}} \rangle, \quad (13)$$

between two concentric shells, where $\langle T_{\text{out}} \rangle$ and $\langle T_{\text{in}} \rangle$ are the mean emission within shells of thickness ΔR outside and inside a spheroidal surface respectively. We then parameterise this spheroid by

$$\left(\frac{x_1}{a}\right)^2 + \left(\frac{x_2}{b}\right)^2 + \left(\frac{x_3}{c}\right)^2 = 1, \quad (14)$$

where $a = a_1$ for $x_1 < 0$ and $a = a_2$ for $x_1 > 0$, $b = b_1$ for $x_2 < 0$ and $b = b_2$ for $x_2 > 0$, and $c = c_1$ for $x_3 < 0$ and $c = c_2$ for $x_3 > 0$. To estimate the shape of the HII region we therefore maximise the quantity T_{contrast} by varying the parameter set $\mathbf{p} = (a_1, a_2, b_1, b_2, c_1, c_2)$. We assume $\Delta R = 1$ Mpc and that the spheroid is centered on the quasar (we also assume the position and redshift of the quasar has been accurately measured by optical/IR observations). In order to evaluate the prospect of measuring the shape of a quasar HII region, this maximisation is performed in the

Table 2. Values of recovered neutral fraction for the four foreground models. The model values are listed in parentheses.

model	index	evolving IGM	non-evolving IGM
I	$n_{\log} = 2$	0.07 (0.15)	0.10 (0.14)
II	$n_{\log} = 3$	0.07 (0.15)	0.10 (0.14)
III	$n_{\log} = 4$	0.04 (0.15)	0.04 (0.14)
IV	$n_{\text{lin}} = 4$	0.04 (0.15)	0.05 (0.14)

noisy, foreground subtracted data sets shown in Figures 1 and 2.

The resulting optimised spheroids are plotted over both model and foreground subtracted noisy maps in Figures 1 and 2. The numerical values of the fitted parameters \mathbf{p} are listed in Table 1. Although the maximisations were performed in the foreground removed maps, the shapes of the recovered HII regions faithfully represent the input model. For example, in the evolving IGM model (Figure 2) the fitted spheroid describes the extension of the observed HII region towards the observer along the (negative) x_3 -direction. This faithful reproduction holds for both the non-evolving and evolving models, and indicates that foreground removal does not erase information regarding HII region shape. To quantify this statement we also perform the maximisation of T_{contrast} on the corresponding input models and list the resulting parameters \mathbf{p} in Table 1 for comparison. The shape of the HII region, including the asymmetries, are very similar in the two cases. We also calculate the volume-averaged radii $\langle R^3 \rangle^{1/3}$ and list these values in Table 1. The values in parentheses are the offset of the parameters \mathbf{p} with respect to this volume-averaged radius. These offsets are similar between the input model and noisy foreground maps, reaffirming that the foreground removal process does not degrade the ability to measure HII region shape and size.

5.4 Estimate of neutral fraction

Based on the fact that the HII region shape is not known a priori, GW07 investigated the constraints on neutral fraction that could be placed using a narrow beam along the quasar line of sight. However, in the previous section we have argued that the spheroidal shape of the HII region can be accurately reproduced from foreground subtracted maps. We can therefore use the full data cube to determine the contrast of emission that originates from regions that are inside and outside of the HII region respectively, rather than just along one line of sight. To achieve this we fit planes of 21-cm emission

$$T_{\text{in}}(\mathbf{x}) = \bar{T}_{\text{in}} + A_{\text{in}} x_1 + B_{\text{in}} x_2 + C_{\text{in}} x_3 \quad (15)$$

and

$$T_{\text{out}}(\mathbf{x}) = \bar{T}_{\text{out}} + A_{\text{out}} x_1 + B_{\text{out}} x_2 + C_{\text{out}} x_3 \quad (16)$$

to regions of the simulations of foreground subtracted 21-cm intensity $T(\mathbf{x}) = T_{\text{obs}}(\mathbf{x}) - T_{\text{fg}}(\mathbf{x})$ that are inside and outside the HII region respectively. This method was adopted in order to fit for both the mean value and evolution of global neutral fraction. Using these solutions we can estimate the global mass-averaged neutral fraction at the redshift of the

quasar, which is obtained from

$$x_{\text{HI}} = \frac{\bar{T}_{\text{out}} - \bar{T}_{\text{in}}}{22\text{mK}} \left(\frac{1+z}{7.5} \right)^{-1/2}. \quad (17)$$

Performing these fits for the models shown in Figures 1 and 2 gives $x_{\text{HI}} = 0.10$ and 0.07 respectively (see Table 2). Ideally, the coefficients $A_{\text{in/out}}$ and $B_{\text{in/out}}$ should vanish. The value of $\Delta C = C_{\text{out}} - C_{\text{in}}$ could in principle be used to measure the evolution in global neutral fraction, however noise and foreground removal will prevent this measurement in practice.

For comparison, we have also computed the corresponding neutral fractions from fits to the input model, which yield values of $x_{\text{HI}} = 0.14$ and 0.15 respectively. Thus, foreground removal erases a significant fraction of the contrast between the HII region and the IGM, which quantifies the observations made from inspection of Figures 1 and 2 in earlier sections. We note that the fraction of contrast that is lost differs between these two examples, owing to the large difference in evolutionary properties of the IGM. This suggests that the effect of foreground removal on the inferred neutral fraction could only be reliably estimated via detailed numerical modelling.

6 SENSITIVITY TO THE FOREGROUND REMOVAL MODEL

Before concluding, we investigate the effect of different foreground removal models on the HII region observables. Specifically, in addition to model II ($n_{\log} = 3$), we choose polynomials in $\log_{10}(\nu)$ with $n_{\log} = 2$ (labelled model I, corresponding to the form of the assumed synchrotron foreground) and $n_{\log} = 4$ (labelled model III). We also consider a polynomial in ν [as opposed to $\log_{10}(\nu)$] of degree $n_{\text{lin}} = 4$ (labelled model IV).

We find that results for the parameters \mathbf{p} describing the shape of the HII region are insensitive to the foreground model, and so have not listed additional results for models I, III and IV. However we find that the neutral fraction derived from observation of an HII region is sensitive to the foreground model assumed, and list these results in Table 2. Models I and II (with $n_{\log} = 2$ and 3 respectively) yield the same neutral fraction ($x_{\text{HI}} = 0.07$ and 0.10 for evolving and non-evolving models respectively). However, the models of higher order (models III and IV) remove additional contrast from the HII region, leading to smaller recovered neutral fractions. This indicates that a model which provides for fluctuations that are of a higher order than those present in the true foreground will lead to removal of power from the inferred 21-cm signal. This in turn implies that the foregrounds will need to be very well understood in order to make quantitative measurements of the neutral fraction based on the observation of HII regions.

7 CONCLUSION

One of the primary goals of future low-frequency telescopes is the detection of large quasar-generated HII regions in redshifted 21-cm emission during the epoch of reionisation. Like all 21-cm signatures of the reionisation era, the detection of

a quasar HII region will need to overcome the difficulties associated with the removal of bright Galactic and extragalactic foregrounds. In this paper we have assessed the impact of removing a spectrally smooth foreground on the observable properties of high-redshift quasar HII regions. We have assumed prior removal of extragalactic point sources and considered only the unpolarised Galactic synchrotron foreground.

The primary effect of continuum foreground removal is to erase contrast in the image. In particular, contributions to the 21-cm intensity fluctuations that have a scale length comparable to the frequency bandpass of the observation are removed by foreground subtraction. On the other hand, we find that this loss of contrast does not affect the ability of 21-cm observations to measure the size and shape of the HII region. We model the HII region shape as a spheroid described by six parameters and show that the shape recovered following foreground removal agrees well with the shape derived directly from fitting using the input model.

Using the recovered best-fit shape of the HII region, the global neutral fraction of hydrogen in the IGM could be measured directly from the contrast in intensity between regions that are within and beyond the HII region. However, we find that since foreground removal lowers the observed contrast between the HII region and the IGM, such a measurement of the neutral fraction would require a correction factor. Our results suggest that the value of this correction factor depends on the reionisation history. This correction factor would therefore need to be modeled using uncertain astrophysics. In addition, the measured contrast of the HII region, and therefore the inferred neutral fraction, is sensitive to the degree of the polynomial used for the foreground removal. Thus, measurement of the neutral fraction from quasar HII regions will require a detailed knowledge of the continuum foreground spectrum.

Finally, we have considered both cases where the quasar is observed in an IGM which evolves slowly relative to the light crossing time of the HII region, and where the IGM evolves rapidly. The latter case is likely to be more relevant for observations around high-redshift quasars which are observed to be very rare at $z > 6$. Our results indicate that the evolution of the IGM will not impact negatively on the ability of 21-cm observations to measure the size and shape of quasar HII regions.

Acknowledgments PMG acknowledges the support of an Australian Postgraduate Award. The research was supported by the Australian Research Council (JSBW). NP and SPO acknowledge support from NSF grant AST-0407084 and NASA grant NNG06H95G.

REFERENCES

Barkana R., Loeb A., 2001, *Phys. Rep.*, 349, 125
 Barkana R., Loeb A., 2005, *ApJL*, 624, L65
 Bharadwaj S., Ali S. S., 2005, *MNRAS*, 356, 1519
 Bock D. C.-J., Large M. I., Sadler E. M., 1999, *AJ*, 117, 1578
 Bowman J. D., Morales M. F., Hewitt J. N., 2006, *ApJ*, 638, 20
 Ciardi B., Madau P., 2003, *ApJ*, 596, 1

Datta K. K., Bharadwaj S., Choudhury T. R., 2007, *MNRAS*, 382, 809
 Di Matteo T., Perna R., Abel T., Rees M. J., 2002, *ApJ*, 564, 576
 Fan X., Strauss M. A., Becker R. H., White R. L., Gunn J. E., Knapp G. R., Richards G. T., Schneider D. P., Brinkmann J., Fukugita M., 2006, *AJ*, 132, 117
 Furlanetto S. R., 2006, *MNRAS*, 371, 867
 Furlanetto S. R., Zaldarriaga M., Hernquist L., 2004, *ApJ*, 613, 16
 Geil P. M., Wyithe S., 2007, *ArXiv e-prints*, 0708.3716
 Gnedin N. Y., Fan X., 2006, *ApJ*, 648, 1
 Gnedin N. Y., Shaver P. A., 2004, *ApJ*, 608, 611
 Iliev I. T., Mellema G., Pen U.-L., Merz H., Shapiro P. R., Alvarez M. A., 2006, *MNRAS*, 369, 1625
 Jelic V., Zaroubi S., Labropoulos P., Thomas R. M., Bernardi G., Brentjens M., de Bruyn G., Ciardi B., Harker G., Koopmans L. V. E., Pandey V., Schaye J., Yatawatta S., 2008, *ArXiv e-prints*, 0804.1130
 Kohler K., Gnedin N. Y., Miralda-Escudé J., Shaver P. A., 2005, *ApJ*, 633, 552
 Loeb A., Zaldarriaga M., 2004, *Phys. Rev. Lett.*, 92, 211301
 McQuinn M., Zahn O., Zaldarriaga M., Hernquist L., Furlanetto S. R., 2006, *ApJ*, 653, 815
 Mesinger A., Furlanetto S., 2007, *ApJ*, 669, 663
 Mo H. J., White S. D. M., 1996, *MNRAS*, 282, 347
 Morales M. F., Hewitt J., 2004, *ApJ*, 615, 7
 Oh S. P., Mack K. J., 2003, *MNRAS*, 346, 871
 Shaver P. A., Windhorst R. A., Madau P., de Bruyn A. G., 1999, *A&A*, 345, 380
 Spergel D. N. et al. 2007, *ApJS*, 170, 377
 Tegmark M., Eisenstein D. J., Hu W., de Oliveira-Costa A., 2000, *ApJ*, 530, 133
 Tozzi P., Madau P., Meiksin A., Rees M. J., 2000, *ApJ*, 528, 597
 Valdés M., Ciardi B., Ferrara A., Johnston-Hollitt M., Röttgering H., 2006, *MNRAS*, 369, L66
 Wang X., Tegmark M., Santos M. G., Knox L., 2006, *ApJ*, 650, 529
 White R. L., Becker R. H., Fan X., Strauss M. A., 2003, *AJ*, 126, 1
 Wyithe J. S. B., Loeb A., 2004, *ApJ*, 610, 117
 Wyithe J. S. B., Loeb A., 2007, *MNRAS*, 375, 1034
 Wyithe J. S. B., Loeb A., Barnes D. G., 2005, *ApJ*, 634, 715
 Wyithe J. S. B., Morales M. F., 2007, *MNRAS*, 379, 1647
 Yu Q., 2005, *ApJ*, 623, 683
 Zahn O., Lidz A., McQuinn M., Dutta S., Hernquist L., Zaldarriaga M., Furlanetto S. R., 2007, *ApJ*, 654, 12
 Zaldarriaga M., Furlanetto S. R., Hernquist L., 2004, *ApJ*, 608, 622